Effect of Cellulose Characteristics on the Properties of the Wet-Spun Aerogel Fibers

applied sciences

MDPI

Article

Effect of Cellulose Characteristics on the Properties of the Wet-Spun Aerogel Fibers

Matin Rostamitabar [1,2], Gunnar Seide [1], Stefan Jockenhoevel [1,2] and Samaneh Ghazanfari [1,2,*]

[1] Aachen-Maastricht Institute for Biobased Materials (AMIBM), Faculty of Science and Engineering, Maastricht University, 6167RD Geleen, The Netherlands; matin.rostamitabar@rwth-aachen.de (M.R.); gunnar.seide@maastrichtuniversity.nl (G.S.); jockenhoevel@ame.rwth-aachen.de (S.J.)

[2] Department of Biohybrid and Medical Textiles (BioTex), AME-Helmholtz Institute for Biomedical Engineering, RWTH Aachen University, 52074 Aachen, Germany

* Correspondence: Samaneh.Ghazanfari@maastrichtuniversity.nl

Abstract: Cellulose aerogels (CAs) from plant or bacterial-derived cellulose have advantages such as low density, high porosity, and high specific surface area and have been used in various applications including biomedical fields. One limiting factor in developing CAs is their demanding shaping process since it involves several steps of dissolution/dispersion of cellulose, geometry configurations using molds or nozzles, coagulation and washing of the gel body, and drying techniques. CA fibers can be converted into textiles and enhance the design ability, stiffness, and flexibility of the CAs. This study aims to understand the correlations between the initial cellulose characteristics, aerogel's internal structure, and its prospective biomedical application. Wet-spun CA fibers were obtained by supercritical CO_2 drying from low and high molecular weight microcrystalline cellulose in calcium thiocyanate tetrahydrate solution. Fiber spinning, thermal behavior, textural properties, and biological assessments of the CA fibers were inspected. The CA microfibers from high molecular weight cellulose proved to have a higher surface area (~197 m^2/g), denser structure, and finer nanofibrils (~2 nm) with better thermal stability in comparison with the fibers produced from low molecular weight cellulose. The fibers were nontoxic, and cell proliferation was observed over time. CA fibers showed promising results to be used for biomedical applications such as tissue engineering and wound care.

Keywords: cellulose; aerogels; fibers; wet-spinning; supercritical CO_2 drying

Citation: Rostamitabar, M.; Seide, G.; Jockenhoevel, S.; Ghazanfari, S. Effect of Cellulose Characteristics on the Properties of the Wet-Spun Aerogel Fibers. *Appl. Sci.* **2021**, *11*, 1525. https://doi.org/10.3390/app11041525

Academic Editor: Hajar Maleki
Received: 11 January 2021
Accepted: 4 February 2021
Published: 8 February 2021

1. Introduction

Aerogels are open pores nanostructured solid networks with high porosity, high specific surface area, and low density [1]. In particular, aerogels are versatile porous materials with tunable textural and morphological characteristics for various fields such as adsorption and separation of materials, thermal insulation, and biomedical application [2–4]. Aerogels morphological characteristics are controllable with various processing parameters such as gelation, shaping, drying, and functionalization [3,5]. Typically, inorganic silica aerogels with very high surface areas (400–1000 m^2/g) are the most well studied and commercially prosperous ones; however, there is an increasing attentiveness to produce aerogels from natural polymers such as cellulose as a sustainable, biodegradable, and often biocompatible resource [6,7].

The drying process of precursor gel aims plays an important role in aerogel fabrication in order to retain 3D porous structure with minimal shrinkage and deformation. Freeze drying and supercritical CO_2 (sCO_2) drying have been widely used in cellulose aerogel (CAs) production; recently ambient pressure drying methods that require physical and chemical modification of the gels have been also studied [8,9]. However, typically sCO_2 dried CAs show better textural and minimal shrinkage in contrast to other drying

methods. Furthermore, sCO_2 processes are mild temperature techniques and favorable for sterilization and bioactive agent loading in biomedical fields [10,11].

Drying in supercritical conditions goes back to 1932 [12]. In the past, supercritical drying was mainly performed in the direct route, which utilized high temperature and pressure supercritical drying of the solvent in the wet matrix. However, these solvents are typically flammable and enhance safety risks. In another method, liquid CO_2 was replaced by the solvent, so-called solvent exchange, and then drying at low supercritical temperature was performed [13].

Since 1994, Bommel et al.'s novel study became a turning point in the supercritical CO_2 drying process [14]. In order to fabricate crack-free silica aerogels, they used this theory that in the case of certain binary mixtures such as ethanol-CO_2, for each temperature, there is a pressure (critical pressure) above which the system is always in a single phase regardless of the composition. Therefore, it provided the chance to use supercritical CO_2 (sCO_2) drying to produce aerogels in milder operation conditions and reduced drying time. Then, the next generation of biomass- and polysaccharide-based aerogels, emerged at the beginning of the twenty-first century which contrary to silica aerogels were less fragile under compression forces [3]. Benefiting from sCO_2 drying, the morphology of the biogel remains reasonably intact or with minimal shrinkage after drying [3,15].

Cellulose, an amphiphilic polysaccharide consisting of linear polymer chains of β-1,4-linked d-glucopyranose molecules, is one of the most abundant natural polymers from renewable resources. Celluloses and its derivatives have widely been used in areas such as conductive materials, energy storage, paper industry, textiles, and pharmaceuticals [16–20]. Furthermore, it is one of the most aged materials that has been used to produce fibers and yarns [21]. Several processes have been described in the literature for the fabrication of cellulose aerogels (CAs) in various geometries of monoliths [22,23], cylinders [24], and beads [25,26] based on different types of cellulose and their derivatives. Fiber and textile production can overcome this designability limitation and enhance the flexibility and mechanical properties of aerogels by fabricating woven or nonwoven textiles from CA fibers and filaments. Furthermore, the fine structure of fibers can decrease the sCO_2 drying processing time from few hours to a couple of minutes since the drying procedure is dependent on the thickness and geometries of the samples.

Various inorganic salt hydrates such as $LiClO_4 \cdot 3H_2O$, $NaSCN/KSCN/LiSCN \cdot 2H_2O$, $Ca(SCN)_2 \cdot 6H_2O$ and $LiCl/ZnCl_2/H_2O$ have been used as efficient agents for dissolving cellulose in a wide range of degrees of polymerization [27]. For the first time, Jin et al. investigated producing CAs monoliths from salt melt hydrate of cellulose and $Ca(SCN)_2 \cdot 6H_2O$ by freeze drying [28]. Hoepfner et al. [21] produced CA fibers based on Jin et al.'s work by spinning a similar solution using a thermally insulated injection device where the fibers were regenerated in an ethanol bath and later dried in sCO_2 as the first fabricated open porous aerogel microfibers using cellulose. Karadagli et al. investigated the spinning dope preparation, extrusion, and characteristics of porous cellulose aerogels fibers from a similar solution and regeneration bath using a micro-extruder and sCO_2 drying [29]. CA fibers have been also fabricated from $ZnCl_2$ salt melt hydrate in similar processing methods in order to investigate their insulation properties in aerospace [30] and automobile applications [31].

Although CAs in other geometrical shapes have been used in multiple biomedical applications such as drug delivery [32,33], tissue engineering scaffolds [34,35], and antibacterial and wound dressing [36,37], the potential of CA microfibers for biomedical application has not been determined. Therefore, the processing, cytotoxicity, and biological assessment of these nanobiomaterials produced by assisting inorganic salts remain essential. This study aims to understand the correlations between initial polysaccharide characteristics, dissolution, and processing of the cellulose using $Ca(SCN)_2 \cdot 6H_2O$ on the final aerogel's internal structure and biological properties. In particular, this research inspects the effect of two different molecular weights of microcrystalline cellulose on the physicochemical and cytotoxicity of the wet spun microfiber CAs that originated from them.

The microcrystalline cellulose and CA fibers are characterized in terms of crystallinity, morphology, physical and textural properties, thermal stability, and cytotoxicity. The CA microfibers produced from high molecular weight powder proved to have a higher surface area and lower crystallinity with a smaller average fibrillar diameter compared to the fibers with lower molecular weight. In comparison to powders, both CA fibers went through cellulose I to cellulose II transformation and were mainly in an amorphous form with lower thermal stability. Fibers were nontoxic and showed cell viability and proliferation as promising indications for using these fibers in biomedical applications where porous fibers are required.

2. Materials and Methods

2.1. Materials

Two different types of microcrystalline cellulose powder with product number C6288 (referred to as C_c) and S6790 (highly purified, referred to as C_s) and calcium thiocyanate tetrahydrate ($Ca(SCN)_2 \cdot 4H_2O$) salt with a purity of 95%, all from Sigma–Aldrich (Darmstadt, Germany), were used in this study. The cellulose powders were dried at 100 °C in a vacuumed oven to remove the moisture. For regeneration and washing the spun fibers, the absolute isopropanol (iPrOH) (≥99.8%, 2-Propanol CP) from Biosolve was used. Carbon-dioxide (CO_2) cylinders (2.7 grade, 50 L) with a purity of 99.7% from Linde Gas Benelux consumed in sCO_2 drying process. Cell proliferation kit II (XTT) was purchased from Sigma–Aldrich. Finally, all materials were used without further purification.

2.2. Solution Preparation, Wet Spinning, and Washing

The salt melt hydrate system of $Ca(SCN)_2 \cdot xH_2O$ ($x \leqq 4$) + yH_2O ($y \leqq 6$) [38] was used to dissolve C_c and C_s. The addition of 2 mol of water to the salt ($Ca(SCN)_2 \cdot 4H_2O$) is necessary to dissolve the cellulose. Homogenous clear solutions were obtained by dissolving C_c and C_s (6% wt.) at 110 °C using a mechanical stirrer (200 rpm) after approximately 25 and 35 min, respectively.

Fiber spinning was done by a customized wet-spinning "LabLineCompact" unit (DIENES Apparatebau GmbH, Germany). The solution needed to be wet spun at temperatures above 80 °C which is the gelation temperature of the solution. Therefore, three heaters with a controller were added to the tank, the pump, and the nozzle pipe. The alcogel fibers (wet alcohol gel bodies) with a diameter of 330 µm were produced using a Dispenstec metal dispensing needle (23AWG, internal diameter 330 µm, 12.7 mm length). Temperature ranges between (110–115 °C), air pressure (2–3 bar), pump rate (1.5 mL/min), winding rate (25–30 rpm) and the iPrOH bath was used to achieve a continuous process for fiber production. The solution solidification in an alcohol bath happened when the temperature of the spun gel decreased from the melting point of the salt to room temperature. Finally, to remove the residual salt from fibers, they were solvent exchanged in 1 L of fresh absolute iPrOH for 5 times. The presence of salt leftover was checked by conductivity meter and spot test. The spot test was performed with iron (III) nitrate (1% wt. v^{-1}) since thiocyanate ions react with iron (III) ions in the solution and form an intense, red-colored complex ion.

2.3. Supercritical CO_2 Drying

The drying procedure was performed using supercritical CO_2 dryer HPE 300 (EUROTECHNICA, Bargteheide, Germany). The fabricated alcogel fibers were wrapped in the filter papers and placed in the vessel (V = 400 mL) with a defined excess amount of iPrOH. Samples were dried at 120 bar and 50 °C over 60 min. During the drying process, the extraction valve of the vessel was manually opened to vent the alcohol-rich mixture of CO_2 into a plastic flask while the pressure and temperature of the vessel remained constant. The extraction cycle of the alcohol rich stream was repeated 5 times for a duration of 3 min. In the end, the vessel was depressurized by a backpressure regulator over 30 min, and the vessel was opened when it cooled down to room temperature. The fibers were instantly

placed in a tightly sealed sample holder under a dry N_2 purge to prevent the samples from absorbing the moisture.

2.4. Size Exclusion Chromatography (SEC)

Size Exclusion Chromatography (SEC) was carried out on cellulose powders with an Agilent 1200 Series LC Equipment (SEC pump G1310A, RI detector G1362A, columns: PSS Gram30 and PSS Gram1000 in series, flow rate: 1 mL min^{-1}; eluent for cellulose samples: DMAc/LiCl). The calibration was done with pullulan standards. Cellulose dissolution in DMAc/LiCl is reported to remain stable over a long time and avoids the degradation of cellulose during the dissolution process; therefore, it is a reasonable solvent for SEC measurement [39].

2.5. Fourier Transforms Infrared Spectroscopy (FTIR)

The Fourier transform infrared spectroscopy technique is one of the useful methods to study the structure of cellulose and regenerated fibers. Fourier Transform Infrared (FTIR) spectroscopy was performed on the powders and fibers with an FT-IR/NIR unit (Perkin Elmer, Waltham, MA, USA). The spectrum was averaged over 32 spectra with a resolution of 2 cm^{-1} from a range of 4000 till 500 cm^{-1} in the reflectance mode.

2.6. X-ray Diffraction (XRD)

Two-dimensional (2D) wide-angle X-ray diffraction (WAXD) analysis was performed on the samples using a SAXSLAB Ganesha diffractometer (SAXSLAB, Denmark), with a sample-to-detector distance of 116.536 mm using Cu Kα radiation (λ = 1.5406 Å) and silver behenate (d_{001} = 58.380 Å), and calibration standard measured for 600 s.

The crystallinity index percentage (CrI (%)) was calculated for all samples by the empirical approximation method of Segal et al. [33] as expressed by the following equation:

$$\mathrm{CrI}(\%) = \frac{I_{002} - I_{\mathrm{amorphous}}}{I_{002}} \quad (1)$$

where for cellulose I, I_{002} is the maximum intensity of the (002) lattice diffraction at $2\theta \approx 22.6^{\circ}$, representing the crystalline aspect of the cellulose and $I_{\mathrm{amorphous}}$ is the intensity at $2\theta \approx 18.7^{\circ}$ representing the amorphous part in the cellulose fibers. For cellulose II, $I_{\mathrm{crystallinity}}$ and $I_{\mathrm{amorphous}}$ is the intensity at $2\theta \approx 20^{\circ}$ and 13°, respectively.

2.7. Thermal Stability Test

The thermal behavior of cellulose powders and produced fibers was investigated by a thermo-gravimetric instrument TA Q500 (TA Instruments, New Castle, DE, USA). Samples were heated from 20 °C to 500 °C with a rate of 10 °C/min under a nitrogen purge.

2.8. Imaging, Scanning Electron Microscope and X-ray Microtomography

To observe the morphology and microstructure of the cross-section of CA fibers, the aerogel fibers were broken in liquid nitrogen and coated with a 3 nm thick layer of iridium. Micrograph images of the fibers' cross-sections were acquired by Teneo scanning electron microscope (FEI, Thermo Fisher Scientific, Waltham, MA, USA). All images were obtained using 5 kV voltage at a working distance of 10 mm. The pore size distribution and the average diameter of microfibers and internal nanofibrils were measured by analyzing SEM images using Image J (version 1.8.0_172, NIH, Bethesda, MD, USA). In particular, the cross-section images were binarized using a similar thresholding procedure for all samples after calibrating the precise scale of the pixels in the software. The pore size distribution was calculated in the particle analyses tool with a minimum size of 1 nm and circularity of 25%.

X-ray microtomography (μ-CT) images were obtained using Skyscann 127211MP (Bruker, Billerica, MA, USA) at the source voltage and current of 40 kV and 200 μA with an exposure time of 1.5 s and image pixel size of 0.8 μm. A CTAn analyzer (version 1.18.8.0+,

Bruker) was utilized to calculate the parameters from 2D aerogel structures within three different regions of interest for each sample. In order to visualize 3D images of the samples, CTvox software (version 3.3.0 r1403, Bruker) was used.

2.9. N_2 Adsorption-Desorption

Surface area and porosimetry measurement of aerogel fibers were performed by ASAP™ 2020 (micrometrics, Norcross (Atlanta), GA, USA). The samples were degassed at 80 °C over 24 h and the Brunauer–Emmet–Teller (BET) method was utilized to determine the surface area. The pore size distribution and average pore size were obtained by Barrett-Joyner-Halenda (BJH).

2.10. Cytotoxicity Test

XTT cell proliferation assay was performed on C_c and C_s powders and two CA fibers produced from them [26]. The negative control was a piece of polyethylene tube, and the positive control was dimethyl sulfoxide (DMSO). The skin fibroblast cell viability was measured on the first and third day of culture using absorbance reading. The absorbance was measured in a multimode microplate reader M200 (Tecan, Männedorf, Switzerland). The assessment was performed in three replicates.

2.11. Statistical Analysis

Experimental data are expressed as means ± standard errors (SD). The statistical analysis was done by Originlab (2019 b) using a significance level of $p < 0.05$. Student *t*-test was performed to determine the differences between different time points.

3. Results

3.1. Properties of Microcrystalline Cellulose Powder and Fabricated Fibers

The molecular weight of microcrystalline powders was obtained by SEC. The number average molecular weight (Mn), weight average molecular weight (Mw), z-average molecular weight, and polydispersity or heterogeneity index results from cellulose powder samples are shown in Figure 1 and Table 1. As shown in Figure 1, cellulose type S (C_s) has a higher number and weight average molecular weight and a broader range of molecular weight distribution. The higher molecular weight of C_s led to a 10 min longer dissolution time in the salt melt hydrate compared to the C_c.

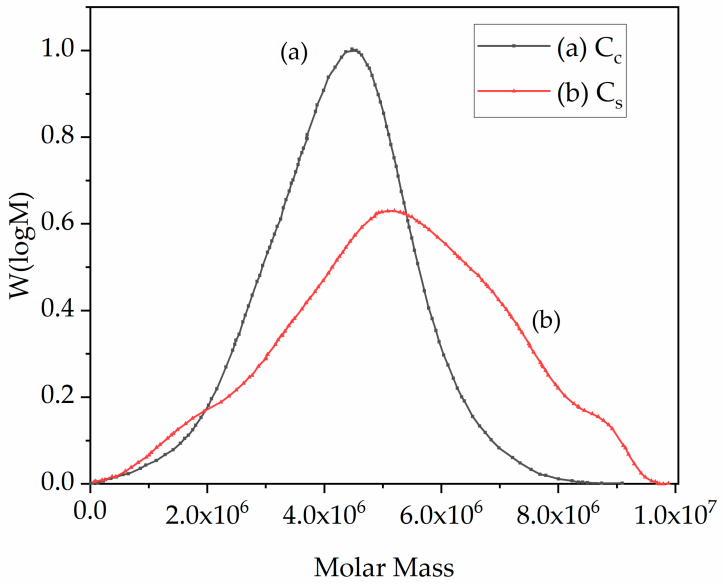

Figure 1. The weight distribution (W(logM)) versus molar mass graphs of microcrystalline cellulose powders were obtained from SEC; cellulose type C (C_c, (a), black) has a narrow distribution of molecular weight while cellulose type S (C_s, (b), red)) has a broader distribution of molecular weight.

Table 1. The result of size exclusion chromatography of cellulose powders C_c and C_s. C_s has a higher molecular weight and polymer dispersity index (PDI).

Sample	Mn (g·mol^{-1})	Mw (g·mol^{-1})	Mz (g·mol^{-1})	PDI
C_c	61,760	163,500	404,220	2.647
C_s	78,700	565,630	1,942,200	7.187

The alcogel fibers (6% wt.) were spun, regenerated, and winded in the regeneration bath around a porous stainless-steel bobbin. No salt leftover was observed because the conductivity for all samples was less than 1 µS/cm and spot tests from all samples were negative and did not show any precipitation of salt. Yellowish-white opaque aerogel fibers were obtained after sCO_2 drying. The fibers obtained from cellulose type C and S are called F_c and F_s, respectively, in the following sections.

3.2. Fourier Transforms Infrared Spectroscopy (FTIR)

Figure 2 shows the FTIR spectra characteristic of the cellulose powders and fabricated CA fibers in the region of 4000–500 cm^{-1}. The cellulose spectra show peaks at 3650–3000 cm^{-1} (O-H hydroxyl group stretching vibration), 2900–2800 cm^{-1} (–CH_2– alkyl stretching vibration), 1645 cm^{-1} (C=O stretching), and 1020 (C–O stretching). Furthermore, the crystalline structural alteration of cellulose from cellulose I to cellulose II were studied with the investigation of the peaks of 897, 1107, 1161, and 1430 cm^{-1} absorption bands, which were assigned to group C_1 frequency, ring asymmetric stretching, C–O–C asymmetric stretching, and CH_2 symmetric bending vibration mainly in cellulose I, respectively [40].

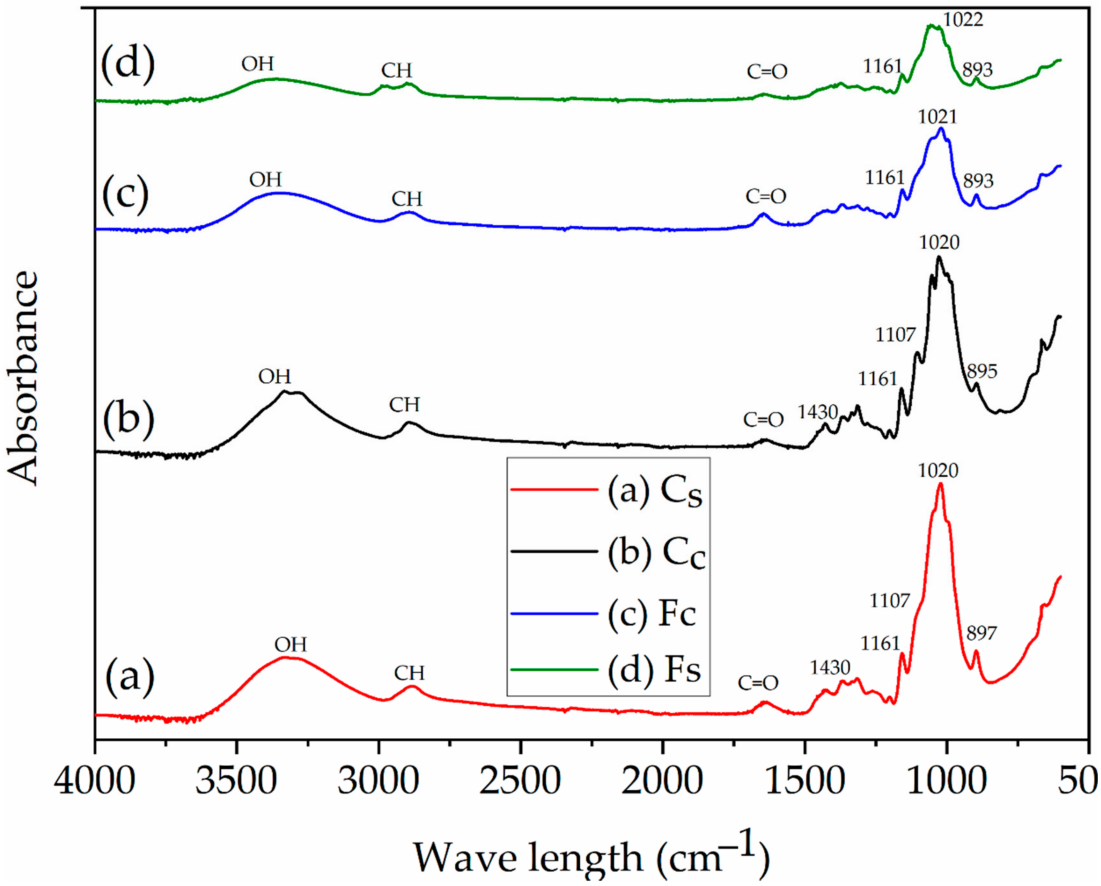

Figure 2. The Fourier transform infrared spectra of cellulose powders (C_s, (a), red and C_c, (b), black) and wet-spun CA fibers (F_c, (c), blue and F_s, (d) green).

Moreover, the 893 cm^{-1} absorption band (β-glucosidic linkages between the sugar units) also confirms that the crystalline cellulose I can be almost negligible in the regenerated cellulose fibers since the 893 cm^{-1} is assigned to group C1 frequency in cellulose II [41,42]. Besides, the typical vibrations in amorphous cellulose at 1260 and 1460 cm^{-1} are similar to those in cellulose in the hydrated melts.

3.3. Wide-Angle X-ray Diffraction (WAXD)

The XRD diffractogram of C_c and C_s with CA fibers generated from them, along with the detector image of the relative microcrystalline cellulose are displayed in Figure 3. Five major diffraction peaks at 2θ = 14.9° (101), 15.9° (101), 21° (021), 22.4° (002), and 34.5° (004) are observed for the microcrystalline cellulose which is in line with values known in the literature for cellulose [40]. However, the CA fibers show a diffractogram with the absence or significant reduction of all peaks corresponding to planes (101), and (002), the values of the Bragg angle characteristic of cellulose I, specifying an amorphous structure. Furthermore, the aerocellulose patterns display peaks in 2θ = 13° and 20° which is the corresponding characteristic of cellulose II [27,43]. It is also explicit that C_c had sharper peaks at (002) as well as more intense regions of radiation absorbance in the detector image and therefore higher crystallinity (Figure 3a) in contrast to C_s (Figure 3b) [44]. The crystallite index for the C_c, F_c, C_s, and F_s was 81.15, 27.58, 42.13, and 12.78 (%), respectively. Therefore, it demonstrates that the degree of crystallinity of the F_c and F_s was extremely lower than of the original cellulose powder, but F_c had higher crystallinity than F_s.

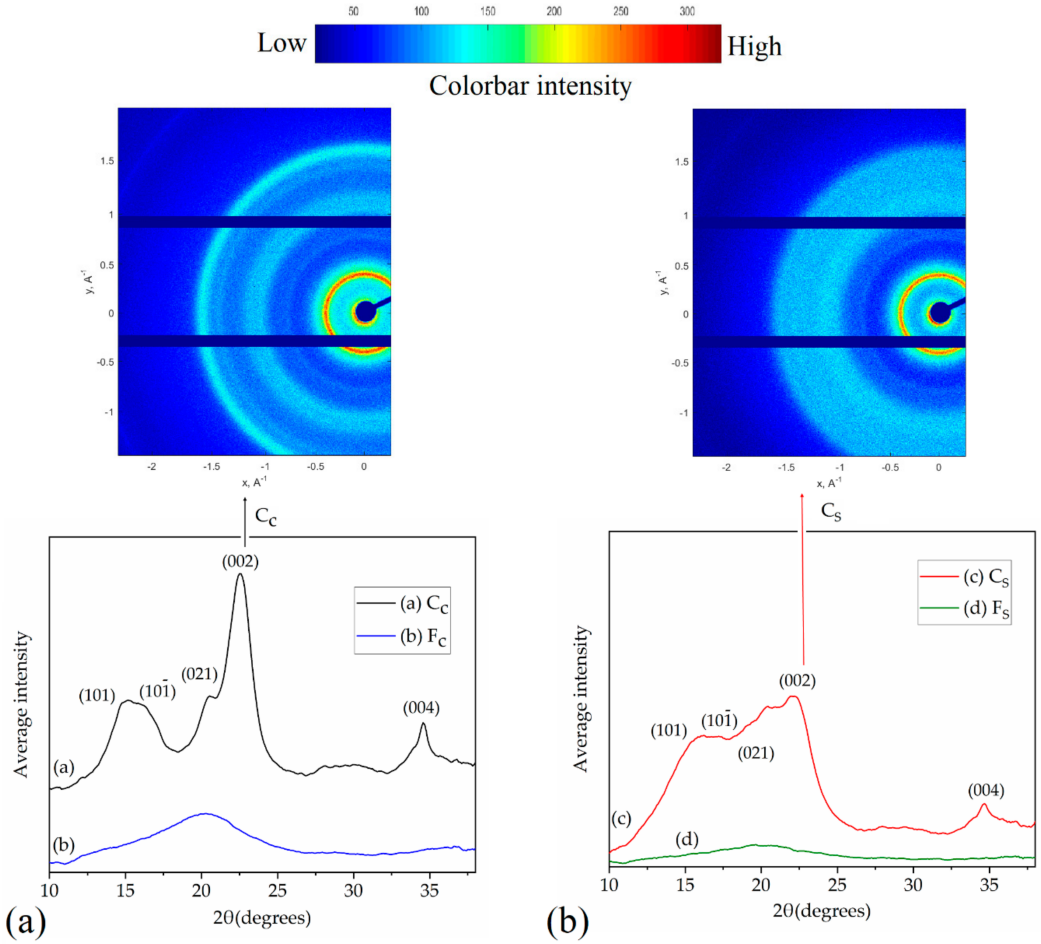

Figure 3. (**a**) The XRD spectra of microcrystalline type C (C_c, (a), black) and originated fiber (F_c, (b), blue) with the detector image of the Cc. (**b**) The XRD pattern of microcrystalline type s (C_s, (c), red) and fabricated fiber (F_s, (d), green) with the detector image of the C_s. C_c had a higher crystallinity index than C_s and fibers regenerated from both cellulose went through cellulose I to cellulose II transformation and formed an amorphous structure.

3.4. Thermal Stability

The thermal behavior and initial decomposition temperature of the cellulose powders and fibers are shown in Figure 4a. The weight loss between 40 and 110 °C was due to the evaporation of the water molecules. Water molecules could have been absorbed on the hydroxyl group of the powder and CA fibers; besides, it is clear that a higher number of water molecules in CA fibers was absorbed in the porous framework [45,46]. From 120 °C to 260 °C, the weight loss was almost unaltered. The weight rapidly decreased from 255 °C to 360 °C because of dehydration and decomposition of the cellulose chains. In derivative thermogravimetry curves (DTG), as shown in Figure 4b, it was indicated that the starting decomposing temperature shifts toward a lower temperature and the maximal weight loss peak was broadened in CA fibers comparing to their initial powder.

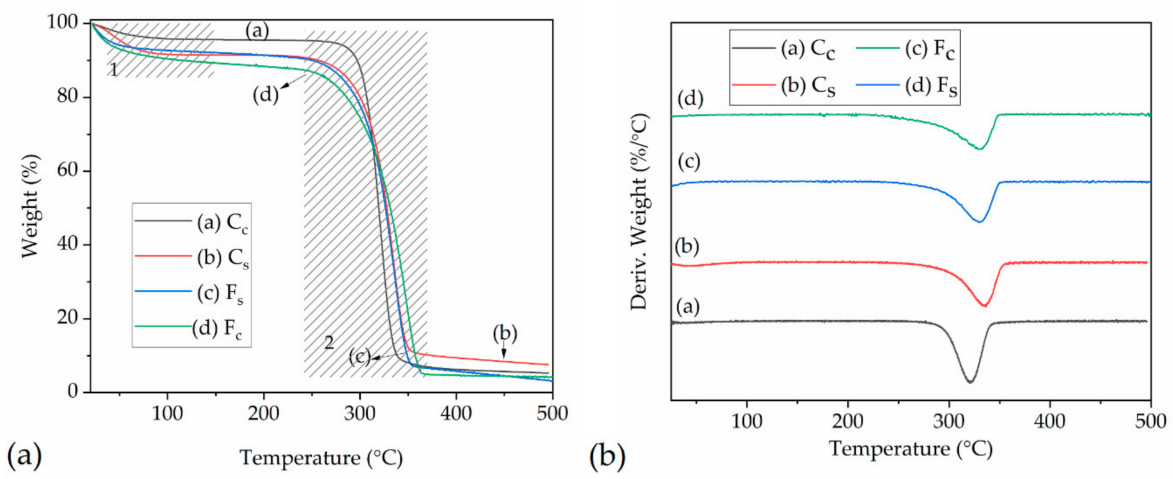

Figure 4. (**a**) TGA graphs of the cellulose powder S (C_c, (a), black), cellulose powders type C (Cs, (b), red) and aerogel fibers type S (F_s, (c), blue) and type C (F_c, (d), green). The first step from 40 to 110 °C in the mass loss was due to the evaporation of water molecules and the second step at elevated temperatures (from 255 to 360 °C) happened due to the relatively fast decomposition of cellulose chains. (**b**) DTG curves show that the decomposing temperature of CA fibers compared to powders shifted toward a lower temperature and the maximal weight peak was broadened.

3.5. Morphology and Textural Properties of the Aerogel Fibers

3.5.1. Imaging by Scanning Electron Microscope

SEM images of the aerogel fibers showed porous meshes of randomly oriented cellulose nanofibrils (Figure 5a,f); the morphology of the fibers is similar to the typical fibrillar cellulose aerogels reported in the literature [21,29]. The image analysis showed more than 60% of the pore sizes are under 5 nm for both fibers (Figure 5g,h); however, few macroscale pores existed for both fibers. Table 2 provides detailed information on the average pore size, minimumand maximum size of the pores in the CA fibers, obtained from SEM image processing.

Furthermore, by measuring the diameter of the microfibers, it was proven that F_c diameter was 275.66 ± 1.24 (μm) while F_s diameter was 281 ± 2.16 (μm). Based on the measured diameters the calculated volume shrinkage of CA fibers after regeneration, washing, and sCO_2 drying was 16.47% and 14.85%, respectively. The diameter of nanofibers in F_s was 22.28 ± 7.61 while F_c had thicker nanofibrils with a diameter of 38.11 ± 7.26 nm.

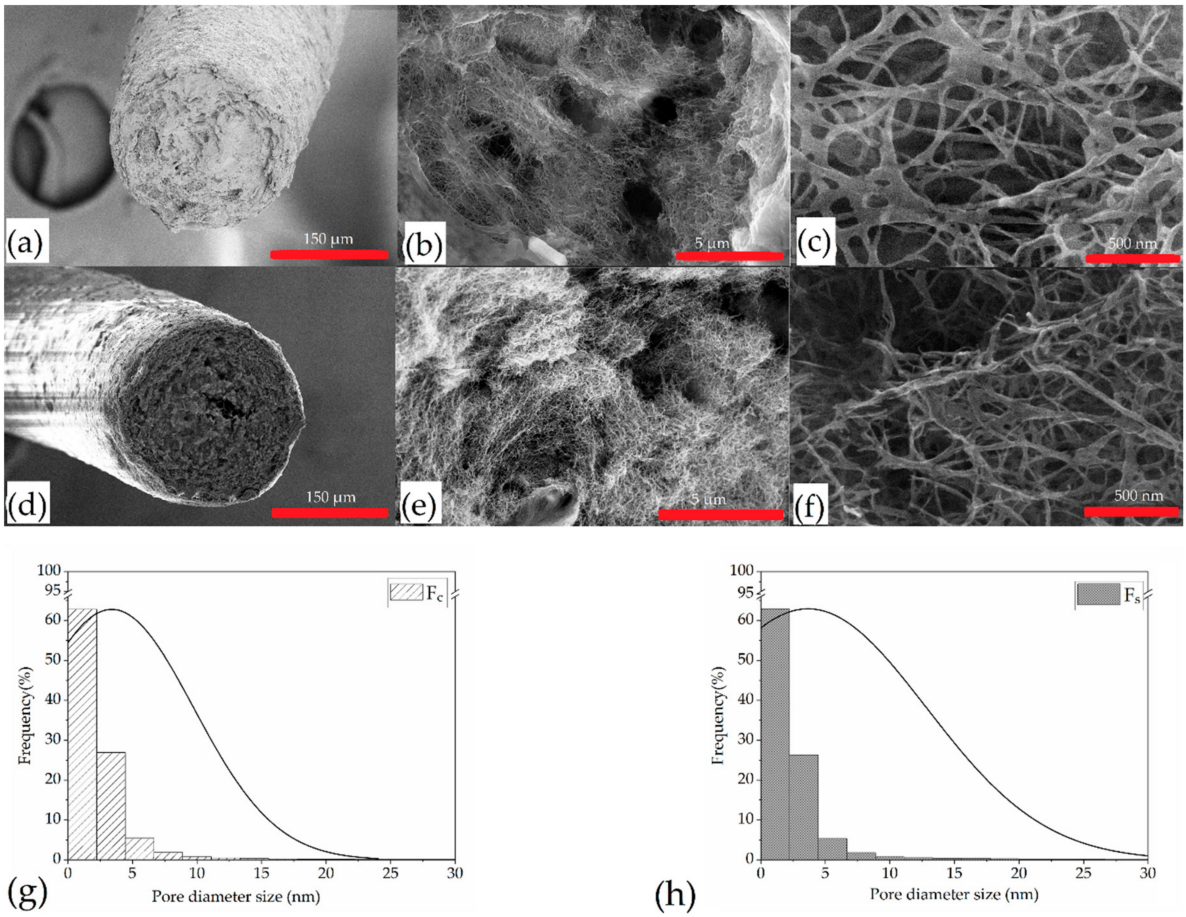

Figure 5. Scanning electron micrographs of the cross-section of cellulose aerogel fibers after regeneration in isopropanol and sCO_2 drying (6 wt.% cellulose content). (**a**) cross-section of F_c (scale bar 150 µm), (**b**) randomly oriented nanofibrils in F_c (scale bar 5 µm), (**c**) cellulose fibrils of F_c (scale bar 500 nm), (**d**) cross-section of F_s (scale bar 150 µm), (**e**) dense and randomly arranged nanofibril in F_s (scale bar 5 µm), (**f**) cellulose fibrils of F_s (scale bar 500 nm). The pore size distribution of F_c (**g**) and F_s (**h**) was acquired by image analysis using Image J software; the analyses showed that more than 60% of the pore sizes were under 5 nm for both fibers.

Table 2. The pore size diameter analysis of F_c and F_s obtained from SEM image processing using Image J software.

Sample	Average Pore Size (nm)	Minimum Size (nm)	Maximum Size (nm)
F_c	3.398 ± 6.346	2.142	1546.107
F_s	3.657 ± 9.165	2.139	2116.107

3.5.2. X-ray Microtomography

µ-CT images showed that fibers from both cellulose types were highly porous and consisted of interconnected open pores structure (Figure 6). The color bar shows the intensity of the X-ray absorbed by the fiber matrix. It was shown by the high intensity (blue-white color) regions that F_s had more condensed regions of nanofibrils. The computed amount of open and closed pores calculated from the image stacks are shown in (Table 3). The F_c has a slightly higher total amount of porosity and open pores compared to the F_s. However, the number of closed pores in both fibers is negligible (<0.01%).

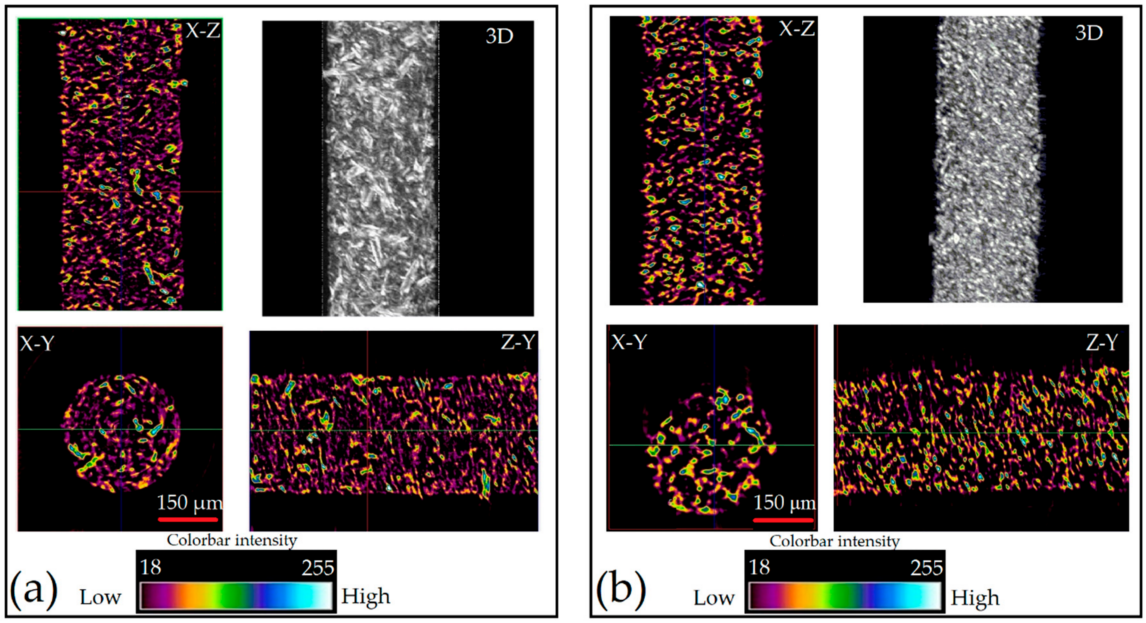

Figure 6. µ-CT images of cellulose aerogel F_c (**a**) and F_s (**b**) in 3 different planes (X-Z, X-Y, Z-Y) with their 3D computed structure. The color bar shows the intensity of the X-ray absorbed by the fiber matrix (min: black and max: white). Scare bar length is 150 µm in all images.

Table 3. The porosity analysis of F_c and F_s obtained by µ-CT assessment using 3D analysis in CTAn software.

Sample	Total Porosity (%)	Closed Porosity (%)	Open Porosity (%)
F_c	77.323 ± 2.331	0.00052	77.32263
F_s	71.649 ± 3.121	0.00575	71.64738

3.5.3. N_2 Adsorption-Desorption

The specific surface area, pore volume, and pore size distribution of the CA fibers was obtained by BET absorption and BJH desorption. The fibers isotherm curves over relative pressure are shown in Figure 7a,b, and incremental pore volume versus pore size width are displayed in Figure 7c and d. The F_s has a higher N_2 quantity adsorbed. The isotherms curves are similar to IUPAC type IV with a hysteresis loop in the range of 0.7–1.0, representing the presence of meso and macroporous structure [47,48]. The multipoint BET specific surface area (SA_{BET}) results showed that F_s had a SA_{BET} of 197 m^2 /g while low molecular weight F_c with the same concentration (6 wt.%) proved to have SA_{BET} of 85 m^2/g. The average nanofibril diameter ($D_{average}$) can be calculated from skeletal density ($\rho_{skeletal}$) and SA_{BET} by the formula $D_{average} = 4/(\rho_{skeletal} * SA_{BET})$, where $\rho_{skeletal}$ is 1.501 g/cm^3 for cellulose [29,47].

The BJH method discovered that majority of pores are distributed under 50 nm in both samples. The dissimilarity was observed over the highest peak of pore size distribution as it was narrower in the F_s and located in the range of 20–30 nm, while the F_c had a broader distribution of pores with a shorter peak height in the range of 20–40 nm (Figure 7d). BJH method clarified that the pore volume of F_s and F_c was 1.03 cm^3/g and 0.36 cm^3/g, respectively; moreover, the BJH desorption average pore width was 19.34 and 17.47 nm for F_s and F_c, respectively.

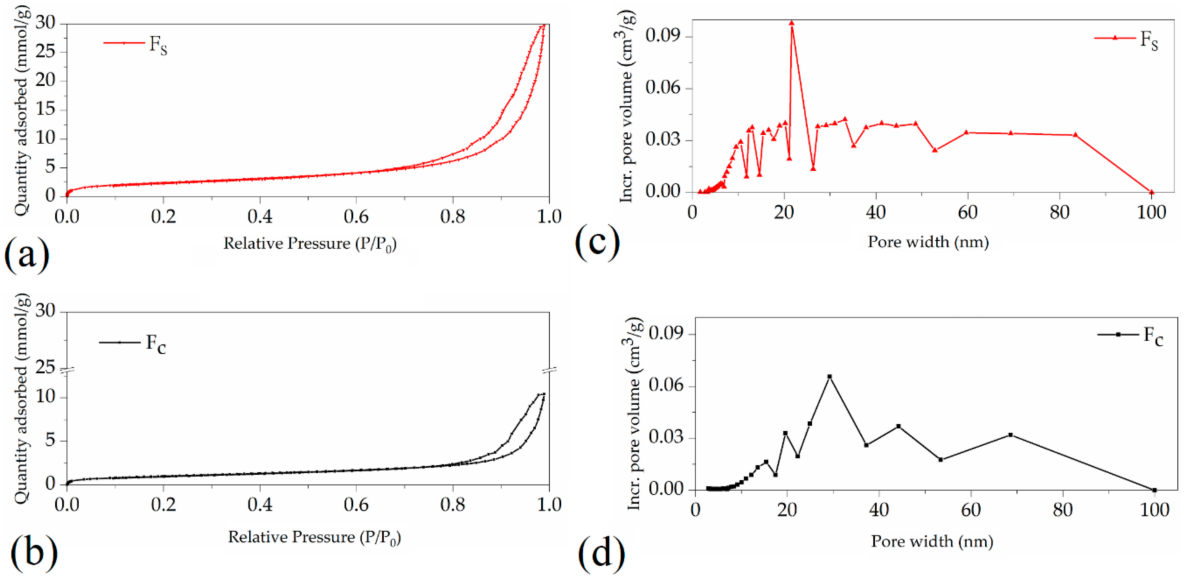

Figure 7. Nitrogen adsorption-desorption isotherms curve and representation of pore size distribution by incremental pore volume versus pore size width of F_s (**a**,**b**) and F_c (**c**,**d**). In contrast to F_c, the F_s had a higher N_2 quantity adsorbed. The majority of pores were distributed under 50 nm in both samples and F_s had a higher pore volume. The specific surface area of F_s and F_c was 197 m^2/g and 85 m^2/g, respectively.

3.6. Cytotoxicity

The cell viability observed in all samples on the first and third days of cell culture proved that the samples were nontoxic. The proliferation of fibroblast cells from day 1 to day 3 was observed in all samples with the exemption of C_c powder (Figure 8). It was also noted that the viability of F_s is slightly lower than F_c.

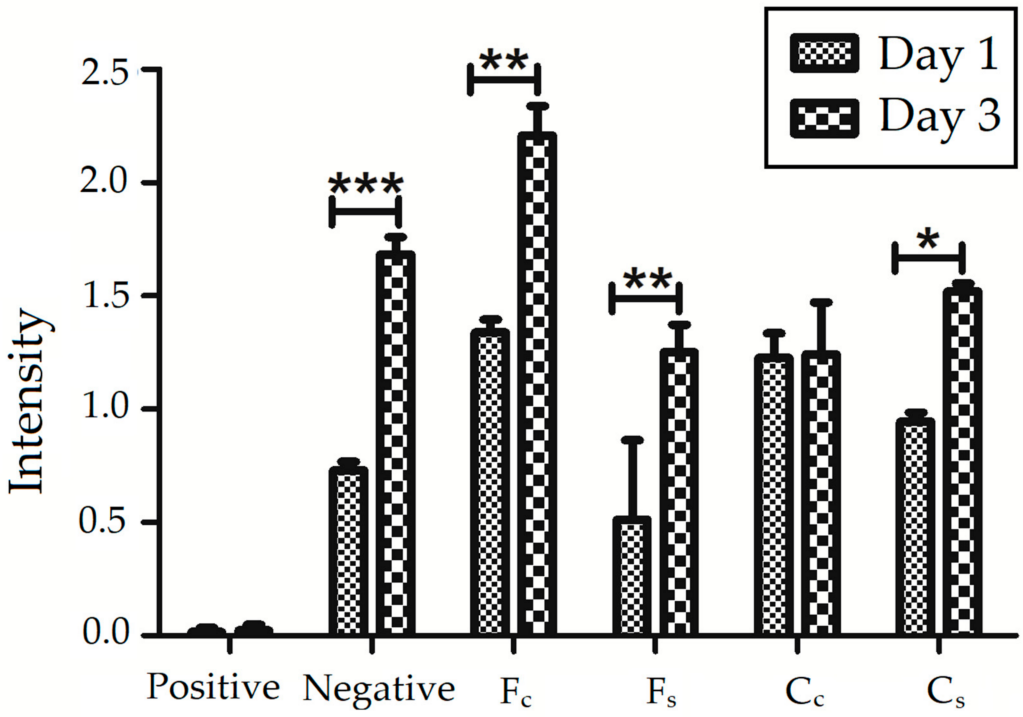

Figure 8. XTT assay of cellulose powders (C_c and C_s) and fabricated alcogel fibers (F_c and F_s). The cell viability was observed in all samples; (***, $p < 0.001$; **, $p < 0.01$; *, $p < 0.05$). Negative samples were polyethylene and positive samples were DMSO. All test samples showed proliferation from day 1 to 3 except C_c.

4. Discussion

The aerogel fibers were fabricated using a semi-pilot scale wet spinning line and utilizing sCO_2 drying unit. sCO_2 processes are gaining more attention in the biomedical field since they are being used as a mild temperature processing method to produce porous materials, such as aerogels, besides being used as a sterilization technique for biomedical products [10]. The significant difference in the type of polysaccharide used for fabricating the aerogels, especially in the structure and length of chains, might have an impact on the morphological properties of fibers because the properties of the cellulosic products rely on the biomacromolecule assembly and its degree of polymerization [49,50]. Two fabricated CA microfibers ($\phi \approx 270$ μm) from low and high molecular weight cellulose exhibited different physical and textural properties in the structural, morphological, thermal, and biological assessment.

The FTIR results proved that the dissolution of the initial biomacromolecule in salt melt hydrate altered the crystalline structure of the material from cellulose I to cellulose II, but no presence of salt leftover was observed. The NCS groups (N bonded) can appear around 2060–2100 cm^{-1}, and SCN groups (S bonded) can appear above 2100 cm^{-1}. As there is no clear peak in the mentioned range of FTIR patterns (Figure 2), it implies that NCS groups are not present in the structure of the fiber after washing steps [51].

Furthermore, XRD showed that the regenerated CA fibers were in the amorphous state and mainly in the form of cellulose II, and F_c had higher crystallinity than F_s as it was originated from high crystalline initial cellulose (C_c). From XRD and FTIR measurements, it can be concluded that the dissolution and the spinning of cellulose in $Ca(SCN)_2$ molten salt hydrate did not change the cellulose chemical structure during the dissolution and regeneration but weakened or broke the inter- and intracellulose hydrogen bonding and inevitably deranged the final CA fiber crystalline arrangement [27,43].

The thermogravimetric measurements disclosed that the CA fibers were slightly less thermally stable than their original cellulose powder due to the decrease of initial degradation temperature. This lower thermal stability was based on several elements such as the conversion of cellulose I to cellulose II, degradation of cellulose chains known for cellulose during dissolution in inorganic salts, and higher specific surface area of the CA fibers compared to the powders, which made the internal surface of fibers more prone to thermal degradation [27,38,52].

To reveal structural and textural properties of the CA fibers SEM, μ-CT, and BET/BJH results needed to be integrated as different compartment length scales from nanometer to micrometer existed in the fiber matrix [53]. The SEM and μ-CT outcomes showed that CA fibers consist of randomly ordered nanofibrils with interconnected pore structure. The BET calculated average nanofibril diameters were 13.5 and 31 nm for F_s and F_c, respectively, which were close to the diameter range of the results obtained via SEM image analysis (~20–38 nm). The larger diameter of F_c's fibrils might trigger some small pores to get closer and agglomerate, leading to lower pore volume [34]. The SEM analysis showed that the average pore width quantities in both samples (~3–4 nm) were lower than the obtained results in BJH desorption method (~17–20 nm), but both methods proved that F_s had a higher pore size diameter than F_c. The low percentage of closed pores in both fibers achieved by μ-CT (<0.01%) was in line with the SEM and N_2 adsorption-desorption results. Alongside sCO_2 drying processes, the regeneration solvent is also essential in achieving a low amount of closed pores. Isopropanol was used as the main regeneration and washing solvents since its low surface tension (0.023 N/m) tends to decrease the number of closed pores during supercritical drying; besides, in previous studies, it has been proven the CAs regenerated in iPrOH have higher mechanical properties than other forms of alcohols (e.g., EtOH) [3,30].

BJH desorption results also showed that F_s had significantly higher pore volume (1.03 cm^3/g) than F_c (0.36 cm^3/g). The obtained value for F_c was lower compared to the porosity acquired by μ-CT because of the resolution limitation of the μ-CT technique which will be discussed further. Overall, both fibers have mainly mesoporous structure with few

macroscale pores. Based on the results of the aforementioned methods, F_s originated from the high molecular weight with lower crystallinity cellulose (C_s) led to thinner nanofirbillar formation (SEM, BET/BJH), interconnected pore structure (μ-CT), and higher surface area and pore volume (BET/BJH).

The difference in the results needs to be explained by understanding the sample preparation and measurement basis of each technique. SEM image analysis is limited to 2D and is highly dependent on the settings used during binary image production. Inaccuracy might also arise from the fibers cross-section preparation since even cutting in liquid N_2 can deform the nanofibrillars. Additionally, fibrils are highly sensitive to the electron beam and throughout the imaging process they can form clusters upon applying high voltages (2–5 kV) [54]. In addition, although the μ-CT analyses provide a more in-depth and accurate overview of 3D structures with insight into the closed pores, the resolution of this technique is limited (in this study, 0.8 μm); this can cause errors, such as neglecting nanofibrils, or considering the agglomeration in the fiber matrix, it might fail to obtain a precise internal computed construction.

On the other hand, N_2 adsorption and desorption data based on BET and BJH theory report the pores which are accessible for gas; miscalculations might arise due to nanofibrillar structural changes in the N_2 pressure variation during the measurements causing some errors in pore diameter values [47,53]. In the case of microfiber shapes, this error can be even higher due to brittleness, high electrostatic charges, and the very lightweight nature of samples. After all, to add enough mass of the fibers in the bulb of the test tube, the aerogel fibers might have been compressed by transferring the samples into the bottom of the tube. It is challenging to control the applied compression when the ultralight aerogel microfibers samples were filled in the test tube. More advanced characterization methods, such as nano-CT as a super high-resolution imaging techniques, are required to obtain a better understanding of the textural properties of CA fibers [55].

The difference in the cell proliferation of the powders might arise from their purity. Regarding the CA fibers, the slower cell proliferation in the F_s can be due to minor trapped salt molecules, which can be thoroughly investigated by elemental analysis methods. The nontoxicity and cell proliferation of samples in addition to their open and accessible interconnected porous network are in favor of tissue integration and vascularization and it shows the potential of CA fibers for scaffold or drug delivery applications [50,56]. The textile production from CA fibers will lead to unique constructs with a macro/microporous structure emerging from the space between microfibers and mesoporous structure originating from porosity of each aerogel fiber; this also enhances the surface to volume ratio of the end product which is favorable for transdermal, wound care, and tissue engineering applications [2,57].

In the prospective studies, the processing route could be more optimized to decrease the destruction of initial polysaccharide chain length and crystallinity as it led to a reduction in the physical and mechanical properties of the end products; for instance, ionic liquids with lower melting temperatures can be used as a dissolving agent [3,58]. Furthermore, the development of greener isolation methods to obtain cellulose from plant resources can minimize the toxicity of the powders. Bacterial cellulose can be a promising candidate to replace plant-derived cellulose since it is produced by enzymes leading to a higher molecular weight and more crystalline assembly of cellulose [4].

In general, tunable macro and micro designability, biomimetic structure, nontoxicity and biodegradability introduce these CA fibers and possible outcome textile as promising candidates for several biomedical application including tissues engineering, wound care, and drug delivery. However, in future studies some of their limitations must be improved. For instance, CA fibers are not wet stable and in case of cyclic evaporation of solvent molecules (e.g., changes in humidity) or immersion in liquids and subsequent ambient drying, their internal structure will collapse over time [59,60]. Additionally, the CA microfibers brittleness remains a challenge for further industrial textile production. These are the two main challenges for many biomedical applications which need to be

overcome using physical or chemical modifications such as plasma treatment, layer by layer assembly, crosslinking, etc.

5. Conclusions

Herein, we successfully fabricated two different cellulose aerogel fibers (6 wt.%) from plant-derived microcrystalline cellulose powders. Fibers were prepared by dissolving the cellulose in calcium thiocyanate melt hydrate combined with wet spinning and sCO_2 drying methods. The aerogel fibers showed lower crystallinity and thermal stability in comparison to their original polysaccharides. The result showed that highly porous constructs were fabricated and proved that the properties of the fibers were affected by using different molecular weights of the polysaccharide. The microfiber originated from a high molecular weight with low crystallinity cellulose powder showed thinner fibril diameter (~17 nm), higher surface area (~197m^2/g), and pore volume (~1.03 cc/g) than the microfiber obtained from the low molecular weight with high crystallinity cellulose. Finally, it was confirmed that the cellulose aerogel fibers produced in this study are nontoxic and thus can be used in biomedical application such as tissue engineering and regenerative medicine applications.

Author Contributions: Conceptualization, M.R., G.S., S.J. and S.G.; methodology, M.R.; software, M.R.; validation, M.R., S.G.; formal analysis, M.R.; investigation, M.R.; resources, M.R.; data curation, M.R.; writing—original draft preparation, M.R.; writing—review and editing, M.R. and S.G.; visualization, M.R.; supervision, G.S., S.J. and S.G.; project administration, G.S., S.J. and S.G.; funding acquisition, S.J. and S.G. All authors have read and agreed to the published version of the manuscript.

Funding: This project: as a part of the FibreNet consortium, has received funding from the European Union's Horizon 2020 research and innovation program under the Marie Skłodowska-Curie grant agreement No 764713.

Institutional Review Board Statement: Not applicable.

Informed Consent Statement: Not applicable.

Data Availability Statement: The data presented in this study are available on request from the corresponding author.

Acknowledgments: We gratefully acknowledge the support of Arnold Wilbers from DSM (Geleen, the Netherlands) for μ-CT assessments and Mojtaba Mohseni from DWI (RWTH Aachen, Germany) for N_2 adsorption-desorption measurements.

Conflicts of Interest: The authors declare no conflict of interest. The funders had no role in the design of the study; in the collection, analyses, or interpretation of data; in the writing of the manuscript, or in the decision to publish the results.

References

1. Corrias, A.; Casula, M.; Aegerter, M.; Leventis, N.; Koebel, M.M. Aerogels containing metal, alloy and oxide nanoparticles in dielectric matrices. In *Aerogel Handbook*; Springer: New York, NY, USA, 2010.
2. Montes, S.; Maleki, H. 12—Aerogels and their applications. In *Colloidal Metal Oxide Nanoparticles*; Thomas, S., Tresa Sunny, A., Velayudhan, P., Eds.; Elsevier: Amsterdam, The Netherlands, 2020; pp. 337–399. [CrossRef]
3. Budtova, T. Cellulose II aerogels: A review. *Cellulose* **2019**, *26*, 81–121. [CrossRef]
4. Abdul Khalil, H.P.S.; Adnan, A.S.; Yahya, E.B.; Olaiya, N.G.; Safrida, S.; Hossain, M.S.; Balakrishnan, V.; Gopakumar, D.A.; Abdullah, C.K.; Oyekanmi, A.A.; et al. A Review on Plant Cellulose Nanofibre-Based Aerogels for Biomedical Applications. *Polymers* **2020**, *12*, 1759. [CrossRef] [PubMed]
5. García-González, C.A.; Budtova, T.; Durães, L.; Erkey, C.; Del Gaudio, P.; Gurikov, P.; Koebel, M.; Liebner, F.; Neagu, M.; Smirnova, I. An Opinion Paper on Aerogels for Biomedical and Environmental Applications. *Molecules* **2019**, *24*, 1815. [CrossRef] [PubMed]
6. Zhu, F. Starch based aerogels: Production, properties and applications. *Trends Food Sci. Technol.* **2019**, *89*, 1–10. [CrossRef]
7. De Marco, I.; Reverchon, E. Starch aerogel loaded with poorly water-soluble vitamins through supercritical CO_2 adsorption. *Chem. Eng. Res. Des.* **2017**, *119*, 221–230. [CrossRef]
8. Long, L.-Y.; Weng, Y.-X.; Wang, Y.-Z. Cellulose Aerogels: Synthesis, Applications, and Prospects. *Polymers* **2018**, *10*, 623. [CrossRef]
9. Li, M.; Jiang, H.; Xu, D.; Yang, Y. A facile method to prepare cellulose whiskers—Silica aerogel composites. *J. Sol-Gel Sci. Technol.* **2017**, *83*, 72–80. [CrossRef]

10. Ribeiro, N.; Soares, G.C.; Santos-Rosales, V.; Concheiro, A.; Alvarez-Lorenzo, C.; García-González, C.A.; Oliveira, A.L. A new era for sterilization based on supercritical CO_2 technology. *J. Biomed. Mater. Res. Part B Appl. Biomater.* **2020**, *108*, 399–428. [CrossRef]
11. Champeau, M.; Thomassin, J.M.; Tassaing, T.; Jérôme, C. Drug loading of polymer implants by supercritical CO_2 assisted impregnation: A review. *J. Control. Release* **2015**, *209*, 248–259. [CrossRef] [PubMed]
12. Kistler, S.S. Coherent Expanded Aerogels and Jellies. *Nature* **1931**, *127*, 741. [CrossRef]
13. Tewari, P.H.; Hunt, A.J.; Lofftus, K.D. Ambient-temperature supercritical drying of transparent silica aerogels. *Mater. Lett.* **1985**, *3*, 363–367. [CrossRef]
14. van Bommel, M.J.; de Haan, A.B. Drying of silica gels with supercritical carbon dioxide. *J. Mater. Sci.* **1994**, *29*, 943–948. [CrossRef]
15. Kikic, I.; Vecchione, F. Supercritical impregnation of polymers. *Curr. Opin. Solid State Mater. Sci.* **2003**, *7*, 399–405. [CrossRef]
16. Vermerris, W.; Abril, A. Enhancing cellulose utilization for fuels and chemicals by genetic modification of plant cell wall architecture. *Curr. Opin. Biotechnol.* **2015**, *32*, 104–112. [CrossRef] [PubMed]
17. Festucci-Buselli, R.A.; Otoni, W.C.; Joshi, C.P. Structure, organization, and functions of cellulose synthase complexes in higher plants. *Braz. J. Plant Physiol.* **2007**, *19*, 1–13. [CrossRef]
18. Chu, H.-Y.; Hong, J.-Y.; Huang, C.-F.; Wu, J.-Y.; Wang, T.-L.; Wu, T.-M.; Lee, R.-H. Enhanced photovoltaic properties of perovskite solar cells by the addition of cellulose derivatives to MAPbI3 based photoactive layer. *Cellulose* **2019**, *26*, 9229–9239. [CrossRef]
19. Jyothibasu, J.P.; Kuo, D.-W.; Lee, R.-H. Flexible and freestanding electrodes based on polypyrrole/carbon nanotube/cellulose composites for supercapacitor application. *Cellulose* **2019**, *26*, 4495–4513. [CrossRef]
20. Huang, X.; Liu, Y.; Deng, J.; Yi, B.; Yu, X.; Shen, P.; Tan, S. A novel polymer gel electrolyte based on cyanoethylated cellulose for dye-sensitized solar cells. *Electrochim. Acta* **2012**, *80*, 219–226. [CrossRef]
21. Hoepfner, S.; Ratke, L. *Open Porous Cellulose Aerogel Fibers*; German Aerospace Center: Köln, Germany, 2008. [CrossRef]
22. Hoepfner, S.; Ratke, L.; Milow, B. Synthesis and characterisation of nanofibrillar cellulose aerogels. *Cellulose* **2008**, *15*, 121–129. [CrossRef]
23. Wu, Z.-Y.; Li, C.; Liang, H.-W.; Chen, J.-F.; Yu, S.-H. Ultralight, Flexible, and Fire-Resistant Carbon Nanofiber Aerogels from Bacterial Cellulose. *Angew. Chem. Int. Ed.* **2013**, *52*, 2925–2929. [CrossRef] [PubMed]
24. Gavillon, R.; Budtova, T. Aerocellulose: New highly porous cellulose prepared from cellulose-NaOH aqueous solutions. *Biomacromolecules* **2008**, *9*, 269–277. [CrossRef] [PubMed]
25. Sescousse, R.; Gavillon, R.; Budtova, T. Wet and dry highly porous cellulose beads from cellulose—NaOH—water solutions: Influence of the preparation conditions on beads shape and encapsulation of inorganic particles. *J. Mater. Sci.* **2011**, *46*, 759–765. [CrossRef]
26. Mohamed, S.M.K.; Ganesan, K.; Milow, B.; Ratke, L. The effect of zinc oxide (ZnO) addition on the physical and morphological properties of cellulose aerogel beads. *RSC Adv.* **2015**, *5*, 90193–90201. [CrossRef]
27. Fischer, S.; Leipner, H.; Thümmler, K.; Brendler, E.; Peters, J. Inorganic molten salts as solvents for cellulose. *Cellulose* **2003**, *10*, 227–236. [CrossRef]
28. Jin, H.; Nishiyama, Y.; Wada, M.; Kuga, S. Nanofibrillar cellulose aerogels. *Colloids Surf. A Physicochem. Eng. Asp.* **2004**, *240*, 63–67. [CrossRef]
29. Karadagli, I.; Schulz, B.; Schestakow, M.; Milow, B.; Gries, T.; Ratke, L. Production of porous cellulose aerogel fibers by an extrusion process. *J. Supercrit. Fluids* **2015**, *106*, 105–114. [CrossRef]
30. Schulz, B.; Meinert, T.; Bierbüsse, D.; Busen, M.; Körtzinger, N.; Stankowski, M.; Seide, G. Cellulose Aerogel Fibers Tested on a REXUS 18 Rocket—The ACTOR Project. *Chem. Ing. Tech.* **2016**, *88*, 1501–1507. [CrossRef]
31. Mroszczok, J.; Schulz, B.; Wilsch, K.; Frenzer, G.; Kasper, S.; Seide, G. Cellulose Aerogel Fibres for Thermal Encapsulation of Diesel Hybrid Engines for Fuel Savings in Cars. *Mater. Today Proc.* **2017**, *4*, S244–S248. [CrossRef]
32. Valo, H.; Arola, S.; Laaksonen, P.; Torkkeli, M.; Peltonen, L.; Linder, M.B.; Serimaa, R.; Kuga, S.; Hirvonen, J.; Laaksonen, T. Drug release from nanoparticles embedded in four different nanofibrillar cellulose aerogels. *Eur. J. Pharm. Sci.* **2013**, *50*, 69–77. [CrossRef]
33. Li, J.; Wang, Y.; Zhang, L.; Xu, Z.; Dai, H.; Wu, W. Nanocellulose/Gelatin Composite Cryogels for Controlled Drug Release. *ACS Sustain. Chem. Eng.* **2019**, *7*, 6381–6389. [CrossRef]
34. Cai, H.; Sharma, S.; Liu, W.; Mu, W.; Liu, W.; Zhang, X.; Deng, Y. Aerogel Microspheres from Natural Cellulose Nanofibrils and Their Application as Cell Culture Scaffold. *Biomacromolecules* **2014**, *15*, 2540–2547. [CrossRef] [PubMed]
35. Zhang, C.; Zhai, T.; Turng, L.-S. Aerogel microspheres based on cellulose nanofibrils as potential cell culture scaffolds. *Cellulose* **2017**, *24*, 2791–2799. [CrossRef]
36. Matsuyama, K.; Morotomi, K.; Inoue, S.; Nakashima, M.; Nakashima, H.; Okuyama, T.; Kato, T.; Muto, H.; Sugiyama, H. Antibacterial and antifungal properties of Ag nanoparticle-loaded cellulose nanofiber aerogels prepared by supercritical CO_2 drying. *J. Supercrit. Fluids* **2019**, *143*, 1–7. [CrossRef]
37. Wang, X.; Cheng, F.; Liu, J.; Smått, J.-H.; Gepperth, D.; Lastusaari, M.; Xu, C.; Hupa, L. Biocomposites of copper-containing mesoporous bioactive glass and nanofibrillated cellulose: Biocompatibility and angiogenic promotion in chronic wound healing application. *Acta Biomater.* **2016**, *46*, 286–298. [CrossRef]
38. Hattori, M.; Koga, T.; Shimaya, Y.; Saito, M. Aqueous Calcium Thiocyanate Solution as a Cellulose Solvent. Structure and Interactions with Cellulose. *Polym. J.* **1998**, *30*, 43. [CrossRef]

39. Sjöholm, E. Size exclusion chromatography of cellulose and cellulose derivatives. In *Handbook of Size Exclusion Chromatography and Related Techniques*; CRC Press: Boca Raton, FL, USA, 2004; Volume 91, pp. 311–354.
40. Poletto, M.; Pistor, V.; Zattera, A.J. Structural characteristics and thermal properties of native cellulose. *Cellul. Fundam. Asp.* **2013**, *2*, 45–68.
41. Nelson, M.L.; O'Connor, R.T. Relation of certain infrared bands to cellulose crystallinity and crystal latticed type. Part I. Spectra of lattice types I, II, III and of amorphous cellulose. *J. Appl. Polym. Sci.* **1964**, *8*, 1311–1324. [CrossRef]
42. Yang, Y.; Zhang, Y.; Lang, Y.; Yu, M. Structural ATR-IR analysis of cellulose fibers prepared from a NaOH complex aqueous solution. *IOP Conf. Ser. Mater. Sci. Eng.* **2017**, *213*, 012039. [CrossRef]
43. Lu, X.; Shen, X. Solubility of bacteria cellulose in zinc chloride aqueous solutions. *Carbohydr. Polym.* **2011**, *86*, 239–244. [CrossRef]
44. Driemeier, C.; Bragatto, J. Crystallite Width Determines Monolayer Hydration across a Wide Spectrum of Celluloses Isolated from Plants. *J. Phys. Chem. B* **2013**, *117*, 415–421. [CrossRef]
45. Ye, S.; He, S.; Su, C.; Jiang, L.; Wen, Y.; Zhu, Z.; Shao, W. Morphological, Release and Antibacterial Performances of Amoxicillin-Loaded Cellulose Aerogels. *Molecules* **2018**, *23*, 2082. [CrossRef]
46. Zhao, T.; Chen, Z.; Lin, X.; Ren, Z.; Li, B.; Zhang, Y. Preparation and characterization of microcrystalline cellulose (MCC) from tea waste. *Carbohydr. Polym.* **2018**, *184*, 164–170. [CrossRef] [PubMed]
47. Reichenauer, G. Structural Characterization of Aerogels. In *Aerogels Handbook*; Aegerter, M.A., Leventis, N., Koebel, M.M., Eds.; Springer: New York, NY, USA, 2011; pp. 449–498. [CrossRef]
48. Smirnova, I.; Gurikov, P. Aerogels in Chemical Engineering: Strategies toward Tailor-Made Aerogels. *Annu. Rev. Chem. Biomol. Eng.* **2017**, *8*, 307–334. [CrossRef]
49. Phillips, G.O.; Williams, P.A. *Handbook of Hydrocolloids*; CRC Press: Boca Raton, FL, USA, 2000.
50. García-González, C.A.; Alnaief, M.; Smirnova, I. Polysaccharide-based aerogels—Promising biodegradable carriers for drug delivery systems. *Carbohydr. Polym.* **2011**, *86*, 1425–1438. [CrossRef]
51. Bertini, I.; Sabatini, A. Infrared Spectra of Substituted Thiocyanate Complexes. The Effect of the Substituent on Bond Type. II. *Inorg. Chem.* **1966**, *5*, 1025–1028. [CrossRef]
52. Chen, W.; Yu, H.; Li, Q.; Liu, Y.; Li, J. Ultralight and highly flexible aerogels with long cellulose I nanofibers. *Soft Matter* **2011**, *7*, 10360–10368. [CrossRef]
53. Maleki, H.; Durães, L.; García-González, C.A.; del Gaudio, P.; Portugal, A.; Mahmoudi, M. Synthesis and biomedical applications of aerogels: Possibilities and challenges. *Adv. Colloid Interface Sci.* **2016**, *236*, 1–27. [CrossRef] [PubMed]
54. Schestakow, M.; Karadagli, I.; Ratke, L. Cellulose aerogels prepared from an aqueous zinc chloride salt hydrate melt. *Carbohydr. Polym.* **2016**, *137*, 642–649. [CrossRef] [PubMed]
55. Kampschulte, M.; Langheinirch, A.C.; Sender, J.; Litzlbauer, H.D.; Althöhn, U.; Schwab, J.D.; Alejandre-Lafont, E.; Martels, G.; Krombach, G.A. Nano-Computed Tomography: Technique and Applications. *Rofo* **2016**, *188*, 146–154. [CrossRef]
56. Coenen, A.M.J.; Bernaerts, K.V.; Harings, J.A.W.; Jockenhoevel, S.; Ghazanfari, S. Elastic materials for tissue engineering applications: Natural, synthetic, and hybrid polymers. *Acta Biomater.* **2018**, *79*, 60–82. [CrossRef]
57. Ozdemir, E.; Sendemir-Urkmez, A.; Yesil-Celiktas, O. Supercritical CO2 processing of a chitosan-based scaffold: Can implantation of osteoblastic cells be enhanced? *J. Supercrit. Fluids* **2013**, *75*, 120–127. [CrossRef]
58. Lindman, B.; Karlström, G.; Stigsson, L. On the mechanism of dissolution of cellulose. *J. Mol. Liq.* **2010**, *156*, 76–81. [CrossRef]
59. Jiang, F.; Hsieh, Y.-L. Dual Wet and Dry Resilient Cellulose II Fibrous Aerogel for Hydrocarbon–Water Separation and Energy Storage Applications. *ACS Omega* **2018**, *3*, 3530–3539. [CrossRef]
60. Cervin, N.T.; Johansson, E.; Larsson, P.A.; Wågberg, L. Strong, Water-Durable, and Wet-Resilient Cellulose Nanofibril-Stabilized Foams from Oven Drying. *ACS Appl. Mater. Interfaces* **2016**, *8*, 11682–11689. [CrossRef] [PubMed]